# Decoding Framework Dynamics in a Spin Crossover Flexible Metal–Organic Framework

Ana Martinez-Martinez, Jorge Albalad, Esther Resines-Urien, E. Carolina Sañudo, A. Lorenzo Mariano, Oscar Fabelo, Jose Alberto Rodríguez-Velamazán, Roberta Poloni, Daniel Maspoch, José Sánchez Costa

# Decoding Framework Dynamics in a Spin Crossover Flexible Metal-Organic Framework

Ana Martinez-Martinez,[a] Jorge Albalad,[b,c] Esther Resines-Urien,[a] E. Carolina Sañudo,[d*] A. Lorenzo Mariano,[f] Oscar Fabelo, [e] Jose Alberto Rodríguez-Velamazán,[e] Roberta Poloni,[f*] Daniel Maspoch[b,c,g] and José Sánchez Costa[a*]

Functional spin crossover (SCO) metal-organic frameworks (MOFs) hold promise for miniaturized spin-based devices due to their tuneable molecule-based properties near room temperature. SCO describes the phenomenon where transition metal ions switch between high spin (HS) and low spin (LS) states upon external stimuli. However, even simple guest molecules like water can significantly alter the properties of these materials. Understanding the interplay between SCO and these molecules is therefore crucial. This work investigates this interplay in a fascinating 3D Fe(II) SCO-MOF, recently reported to exhibit reversible conductivity even in bulk.[44] We employ a combined experimental and computational approach to explore how guest molecule uptake/release influences SCO dynamics including a transition from partial HS/LS to a fully LS state at high temperatures, (named reverse SCO) and ligand disorder-order behaviour. Our findings reveal a solid-state mechanism that differs from those previously described.

## Introduction

Metal-organic frameworks (MOFs) have emerged as a versatile class of materials due to their tuneable properties and potential for a broad number of applications, including gas storage, molecular sensing, catalysis, and electronics.[1–3] Among these, MOFs that exhibit spin crossover (SCO)[4–9]—the ability to switch between the high spin (HS) and low spin (LS) electronic states in response to external stimuli[10] (Fig. 1a)— are particularly attractive for spintronic devices, magnetic sensors,[11,12] energy saving[13] and memory storage systems.[14] SCO transitions are typically driven by changes in temperature,[15] pressure,[16] light exposure,[17,18] or the adsorption/desorption of guest molecules,[19–21] which alter the magnetic and electronic properties of the material.[22–24]

While conventional SCO systems exhibit a LS to HS transition upon heating, there is growing interest in materials that demonstrate the reverse SCO behaviour, where the switch occurs from HS to LS upon heating.[25,26] The reverse SCO is a thermodynamically counterintuitive process, as the more entropic HS state is typically favoured at higher temperatures. This rare phenomenon is generally of low magnetic magnitude and often induced by a crystallographic phase transition.[27] Controlling the reverse SCO offers unique opportunities for designing ON/OFF advanced materials with dynamic magnetic and electronic functionalities.[28]

Beyond temperature, guest molecules have been shown to significantly influence the SCO behaviour[29,30] through: *i)* steric effects that favour the HS state[31–34] reducing the critical transition temperature, and *ii)* electronic effects[35,36] that can either decrease or increase it. The structural adaptability of these materials allows them to respond dynamically to environmental changes, providing a high degree of control over the magnetic properties through simple external stimuli, such as temperature or humidity.[37–39] This flexibility, linked to the reversible nature of solvent uptake and release, can play a central role in the SCO process.[40,41]

In this work we present a comprehensive investigation of 3D MOF, $[Fe_2(H_{0.67}bdt)_3]\cdot xH_2O$ (**1**, where x = 0–10 and $bdt^{2-}$ = 1,4-benzeneditetrazolate),[42–44] which exhibits a reverse spin crossover (SCO) transition upon heating and subsequent dehydration, transitioning from a mixed HS/LS state to a fully LS state. This transition takes place between 343 K and 423 K and involves an increase in the intrinsic electrical conductivity of the MOF. Through a combination of experimental techniques, including single-crystal X-ray diffraction (SCXRD) and adsorption/desorption isotherms, alongside density functional theory (DFT) calculations, we elucidate a novel dynamic mechanism involving the interplay of phenyl ring order-disorder, lattice network changes, solvent accessibility volume and spin state.

This result highlights the importance of the flexibility of the framework and its ability to modulate the spin state based on hydration levels. In addition, the spin state has been shown to affect the charge transport properties of this MOF[44] adding an additional layer of functionality. The ability to manipulate both magnetic and electrical behaviours via the adsorption/desorption of guest molecules—specifically water—underscores the significance of understanding host-guest interactions in MOFs. [45–47]

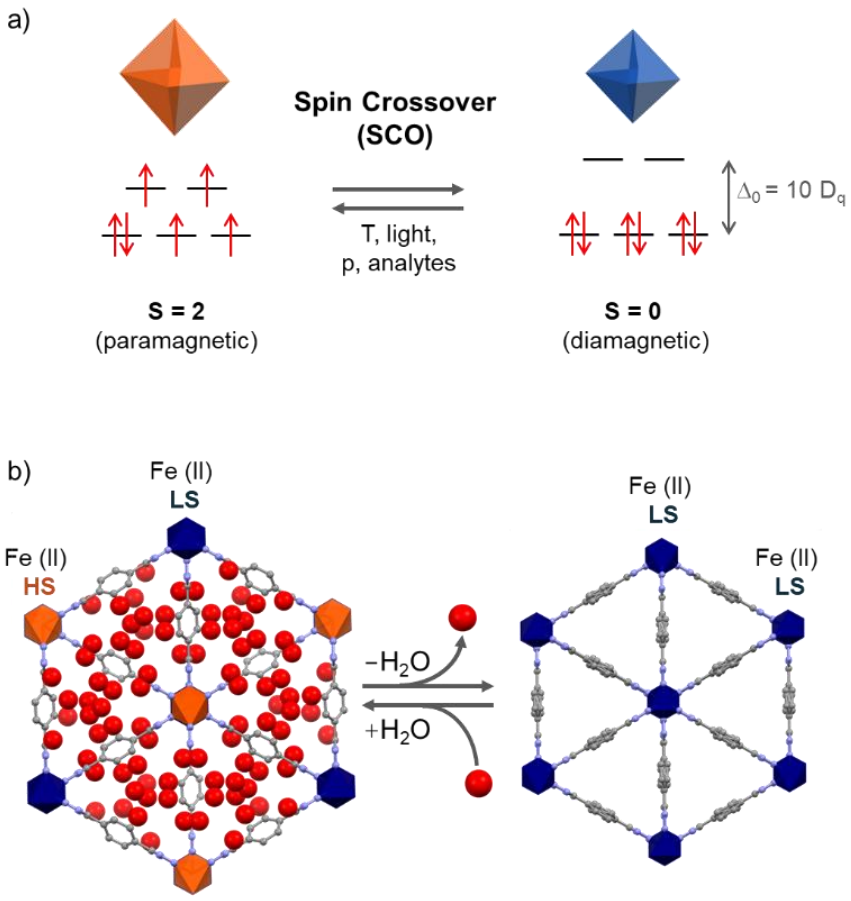


**Fig. 1**. a) Representation of the two spin states of an Fe(II) ion, the HS and the LS electronic states. Under external stimuli, such as temperature, pressure, light irradiation or the inclusion of analytes, the crystal field splitting $\Delta_0$ can be modified and the SCO materials can switch between both electronic states. b) 3D perspective of **1** at room temperature (**1**$^{300}$). LS Fe is represented in dark blue, HS Fe in orange, N in blue, and C in grey. H atoms are omitted for clarity.

## Results and discussion

**Water adsorption/desorption isotherms of 1**

Initially, we performed an adsorption study to investigate the loss/uptake of water molecules of **1**. Fig. 2 shows the water adsorption isotherms measured at room temperature for two consecutive cycles. Note that prior to the first cycle, the crystals were activated at 423 K under vacuum for 12 hours to ensure complete dehydration.

In the first adsorption isotherm, water uptake increased rapidly with increasing $H_2O$ partial pressure ($P/P_0$) up to approximately 0.4. Beyond this point, the uptake gradually reached a total of 23.6% corresponding to 9.8 water molecules per molecular formula. However, during desorption, a hysteresis was observed that did not revert to the original starting point, indicating incomplete desorption. The minimum remaining water content after the first cycle was 3.8%, suggesting that 1.6 water molecules per formula remained strongly adhered within the lattice (Fig. 2a).

A second adsorption/desorption cycle (Fig. 2b) was immediately performed following the first, without any further activation of the sample, starting from the end point of the first cycle, with compound **1** containing 1.6 $H_2O$ molecules in the lattice. Upon completion of adsorption, the mass percentage regained (18.7%) indicates the uptake of 8.1 water molecules, which were completely removed during the desorption cycle. To confirm the behaviour observed in the first isotherm, a third cycle was carried out on the same sample (Fig. S1 and S2†). Before this third cycle, the material was re-activated at 423 K under vacuum for 12 hours. Afterward, the same adsorption and desorption behaviour as in the first cycle was observed.

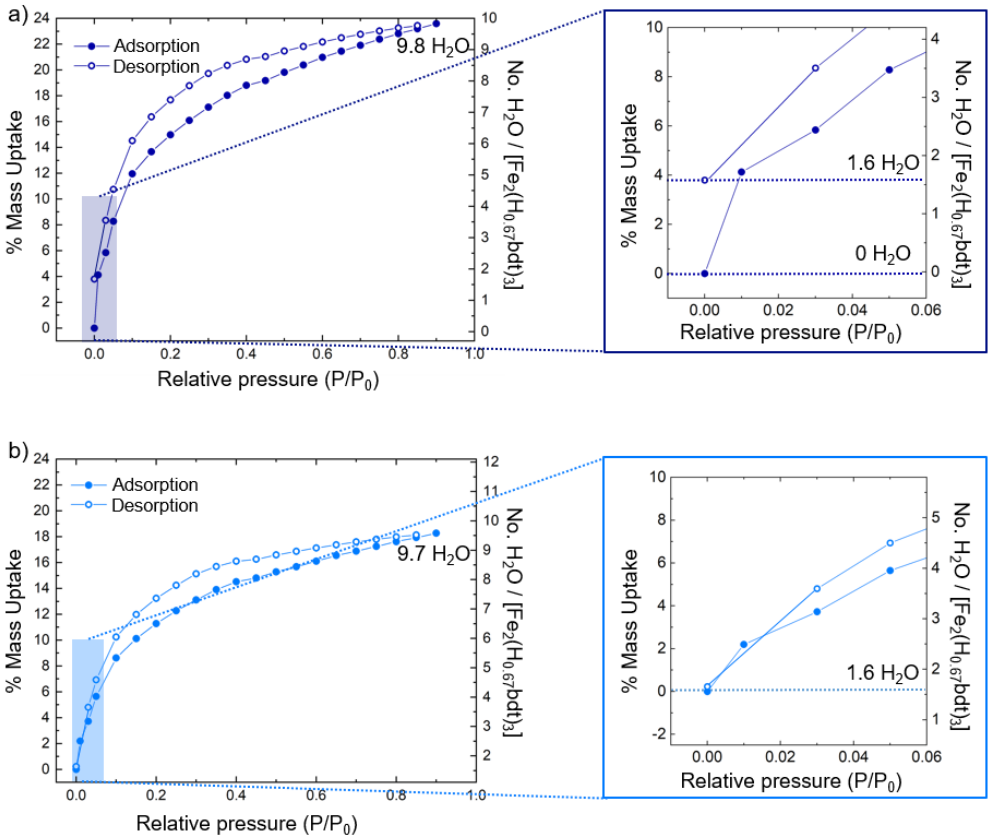


**Fig 2.** a) First water adsorption/desorption cycle at 298 K of crystalline **1**. b) Second water adsorption/desorption cycle at 298 K, immediately after the first without reactivation.

These observations suggest the presence of two distinct water populations within the network. One population is readily adsorbed and desorbed (~8.0-8.5 $H_2O$ per formula), while the other remains tightly bound and requires harsher conditions (vacuum and elevated temperature) to be removed from the lattice (~1.5 $H_2O$ per formula). This result is consistent with the previously reported quantity of water found in the pores of as-synthesized **1**, as determined by TGA.[44] Two different weight losses regions were observed, a sharper decrease up to 350 K (~6 $H_2O$) followed by a more gradual weight loss up to 515 K (~3 $H_2O$) (Fig. S3†).

To further elucidate the relationship between the water molecules and the spin state, magnetic measurements (Fig. S4†) were carried out of **1** as-synthetized, **1** measured after the first adsorption/desorption cycle (~1.5 $H_2O$ per formula) and **1** after submerging the dehydrated crystals in water for 15 days. The product of the temperature-dependant magnetic susceptibility for **1** is around 3 $cm^3 \cdot K \cdot mol^{-1}$, which is in agreement with one Fe(II) centre in the HS state and one in the LS. After the first water isotherm is performed, the $\chi_M T$ product drops to 1.2 $cm^3 \cdot K \cdot mol^{-1}$, concurrent with a partial spin transition of the HS iron centres to the LS. After rehydration, the original $\chi_M T$ value is restored, confirming that the spin transition is caused by the loss of water molecules.

**Single-crystal X-Ray diffraction**

**Unveiling water adsorption sites in 1 at low temperature ($1^{100}$)**

To investigate whether these apparently distinct populations of water molecules are correlated with their position in the structure, the SCXRD structure of **1** was measured at 100 K ($\mathbf{1^{100}}$), where the order of water molecules in the pores is maximal.

Complex $\mathbf{1^{100}}$ crystallizes in the trigonal crystalline system with a total volume of 3207 $Å^3$. The structure extends along the *c*-axis with 1D Fe-tetrazole chains linked by 2,3-bridging tetrazole as illustrated in Fig. 1b. According to the Fe-N bond lengths (Fe1-N1: 1.946 Å and Fe2-N2: 2.098 Å), $\mathbf{1^{100}}$ exhibits a 59 % population of Fe ions in LS and 41 % in HS, in agreement with a partial spin transition induced by temperature cooling.[42]

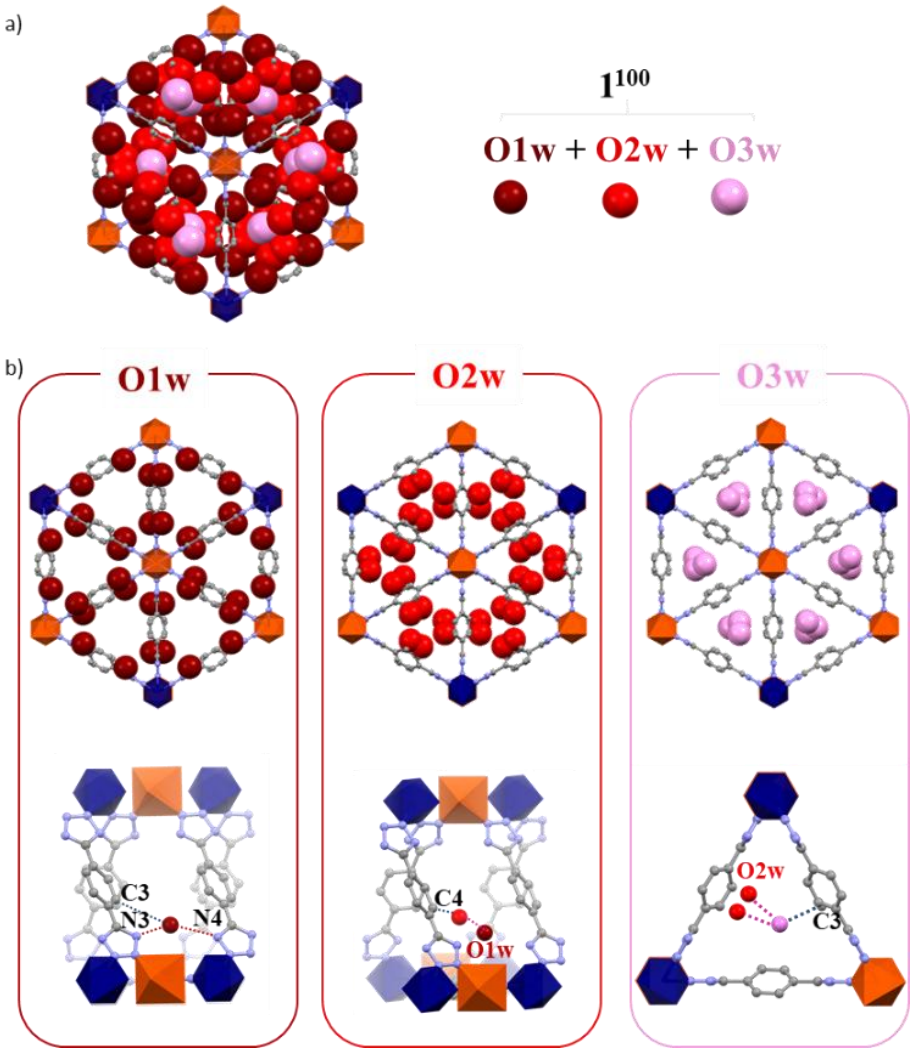


**Fig. 3.** a) Structural representation of $\mathbf{1}^{100}$ filled with the three types of water molecules. b) Spatial organization of each type of water molecule found in $\mathbf{1}^{100}$ and main interactions between the water molecules and the lattice for O1w, O2w and O3w. Interactions between water molecules and the tetrazole moiety are depicted in dark red, interactions between water molecules themselves in green, and water molecules-phenyl rings in light blue.

The analysis of $\mathbf{1}^{100}$ revealed three distinct water molecules (O1w, O2w, and O3w, see Fig. 3). O1w occupies two distinct positions, each with an occupancy of 0.5, forming hydrogen bonds with the tetrazole organic ligand (O1w-N3: 2.833 Å; O1w-N4: 2.915 Å) and interacting with the phenyl ring via dipole-π (shortest distance with the ring: O1w-C3: 2.876 Å). Similarly, O2w occupies two positions with 0.1667 occupancy each. O2w forms a hydrogen bond with O1w (O2w-O1w: 2.415 Å) and interacts with the ligand's benzene moiety (shortest distance: O2w-C4: 2.404 Å). Finally, O3w occupies the centre of the triangular pore, forming a hydrogen bond with O2w (O3w-O2w: 2.769 Å) and interacting with the phenyl group (O3w-C3: 2.773 Å). For complete details, see Table S3† and Fig. S5†.

It is important to remark that in the crystallographic studies, the number of water molecules per formula is lower than that determined with the isotherms, as only the ordered water molecules can be fixed in a specific position.

By correlating the adsorption isotherms with the SCXRD information extracted from the $\mathbf{1}^{100}$ structure, it can be proposed that the easily adsorbed/desorbed water molecules are of the O2w and O3w types, whereas the water molecules that remain attached to the network after desorption are likely of the O1w type, due to the strong hydrogen bonds they form with the tetrazoles.

**SCXRD of 1 under heating process ($\mathbf{1}^{100}$ → $\mathbf{1}^{300}$→ $\mathbf{1}^{350}$ → $\mathbf{1}^{420}$)**

Then, a comprehensive temperature-dependent SCXRD study was conducted to elucidate the structure-property relationship within this MOF. Single crystals of **1** were collected and analysed at 300, 350 and 420 K (detailed information is provided in Fig. 4 and Section 5 of the SI†). This study used the PLATON/SQUEEZE[48] tools to determine the solvent accessible volume (SAV) and electron density (ED) (both expressed by unit cell ($[Fe_6(H_{0.67}bdt)_9]$) in the pores of the structure of $\mathbf{1}^{100}$, $\mathbf{1}^{300}$, $\mathbf{1}^{350}$ and $\mathbf{1}^{420}$. SAV refers to the space within the material where solvent molecules, such as water, can enter and move freely. The ED calculated within the SAV can be correlated with the presence of water molecules (see Fig. 4a and Table S5† for further details). Moreover, the temperature-dependent disorder of the benzyl ring[49] (Fig. 4b) was explored, as it produces a steric hindrance that affects the SAV.

In **$1^{100}$,** the framework volume is 3207 Å and the SAV has a value of 533 Å³**,** where an electron density corresponding to 24 water molecules was found. Furthermore, at this temperature, the phenyl carbons are observed in two different positions (see Fig.4b).
An increase in temperature to 300 K (denoted as **$1^{100} \rightarrow 1^{300}$**) resulted in an expansion of the unit cell volume to 3299 Å³, along with a rise in the HS population to 50 %. This expansion can be attributed to the elongation of Fe-N distances (details provided in Table S2†). At this temperature, the disorder within the benzene rings remained significant, with a slight increase compared to that observed in **$1^{100}$**. However, the SAV increased significantly to 1005 Å³. As no guest water loss occurs at this temperature, the primary contributor to the framework expansion is the spin transition, as the benzene disorder showed only a minor increase (see Fig. 4). The electron density found within the SAV corresponds to 23.4 water molecules, very similar to the number observed at 100 K.
Further heating from **$1^{300} \rightarrow 1^{350}$**, in which a percentage of O2w and O3w water molecule types are released, resulted in a decrease in the framework volume, consistent with the partial transition of iron metal centres to the LS state, 69% LS and 31% HS. Although dehydration is not complete in **$1^{350}$**, the water loss induces flexibility in the framework, significantly decreasing the cell volume to 3069 Å³. This framework contraction leads to a reduction in the SAV to 518 Å³ and coincides with a considerable increase in the disorder of the benzene-ring of the ligands. In addition, the SCXRD structure revealed an out-of-plane configuration for the phenyl carbon atom directly linked to the tetrazole moiety (see Fig. 4b, S6† and Table S4†), likely related to the space created by water release. These combined observations suggest a dynamic adaptation of the organic framework through phenyl ring rotations, with can accommodate both structural contractions and elongations.
Finally, in **$1^{420}$**, the spin transition is complete. At this temperature, likely O2w and O3w water molecule types are all released and O1w type is partially lost. This results in a further decrease in the framework volume to 3015 Å³. The benzene ring configuration adopts a more ordered state, with two closely spaced positions, despite the elevated temperature. This leads to a notable increase in pore accessibility, reaching a value of 915 Å³. The electron density found within the SAV corresponds to 2.4 $H_2O$ molecules per unit cell.
Based on this information, it can be concluded that several factors influence the evolution of pore accessibility in **1** with temperature. One key factor is the reduction of the framework volume as the proportion of metal centres in the LS increases, highlighting the correlation between magnetic behaviour and structural changes (Fig. S8). However, when the temperature reaches 420 K, this decrease in framework volume is accompanied by a very considerable increase in the SAV. Despite the lattice decreasing around 2% (**$1^{350} \rightarrow 1^{420}$**), SAV increases by 43%. This significant increase is due to the benzene unit positioning itself in such a way that it does not sterically hinder the entry of the solvent, making the pore more accessible.

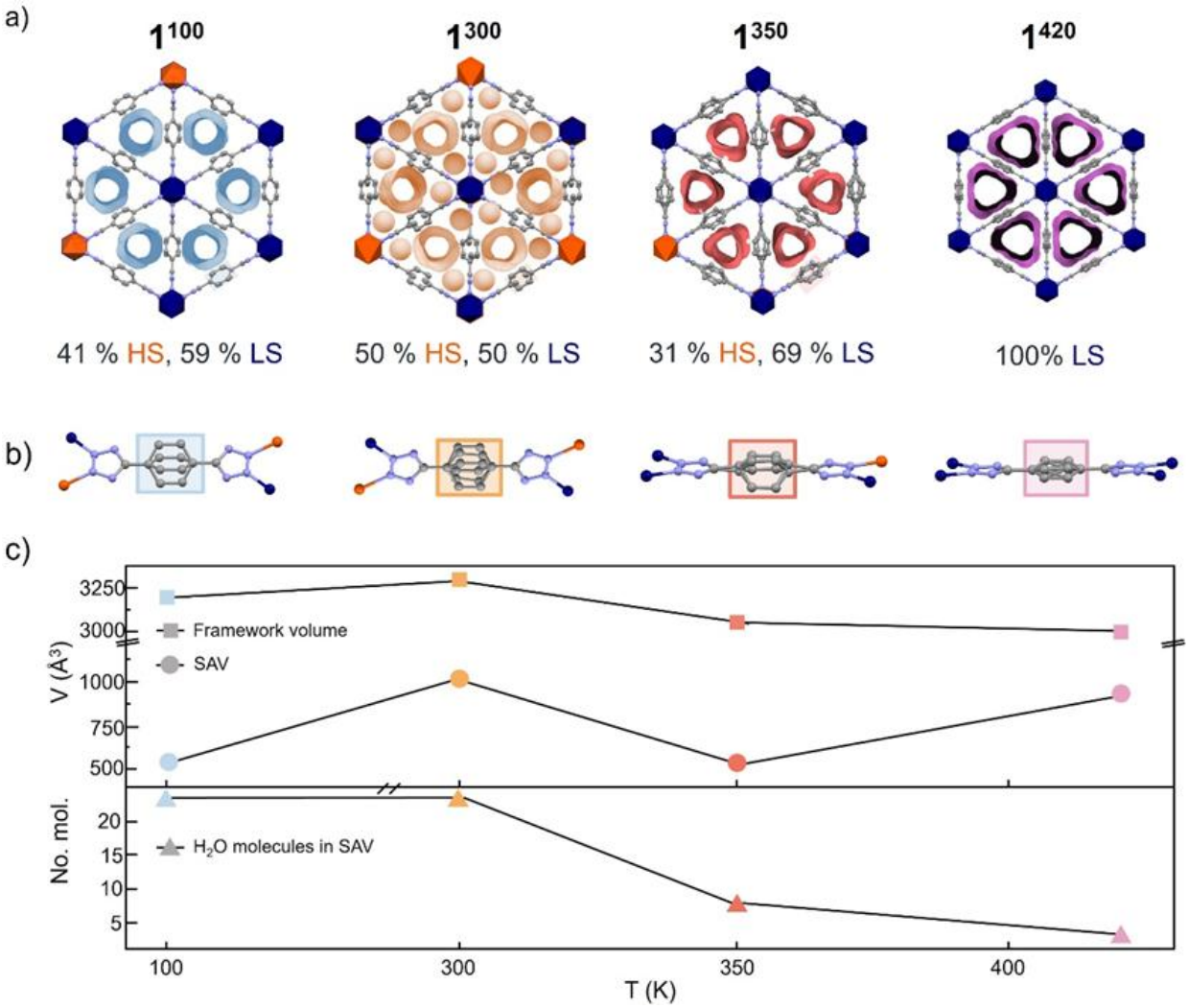


**Fig. 4**. a) Schematic representation of the evolution of the electron density in the pores with temperature. b) Disorder evolution in the benzene ring of the $H_2$bdt ligand with temperature. c) Variation of the framework volume, SAV and the number of water molecules found with temperature.

In the SCO phenomenon, the transition from a HS state to a LS state causes ligands within the crystal lattice to become immobilized in specific positions.[49] This effect is particularly pronounced in ligands with cyclic groups, such as phenyls, which have inherent rotational freedom. The fixation of these ligands occurs mainly due to a reduction in the distance between Fe-donor bonds during the spin transition, which can reach up to 20% (approximately 0.2 Å). This results in a decrease in the volume of the crystal cell and an increase in the electron density in the environment of the ligands, limiting their positional freedom.

In porous materials such as MOFs, when guest molecules -- such as water -- present in the pores are evacuated, the electron density decreases, reducing the steric hindrance around the ligands and, therefore, increasing their rotational capacity.

The SCO-MOF studied in this work exhibits both singularities at once. On one hand, the HS-to-LS transition should immobilize the ligands, restricting their positional freedom, while on the other hand, the evacuation of water molecules from the pores should facilitate the rotation of the phenyl groups. However, the experimental results reveal that as the temperature rises, the positional freedom of the phenyl rings decreases. This indicates that, in this case, the ligand fixation effect induced by the spin transition and the associated reduction of the framework volume predominates over the theoretical increase in positional freedom that would be expected from the evacuation of water from the pores and the increase in the SAV (see high temperature part of Figure 4).

The optimized geometries for both LS and HS/LS states across varying water contents at the O1w position were used to calculate the adiabatic energy difference between the LS and HS/LS configurations. The Hubbard U density-corrected scheme was employed for this purpose (see section S8† for further details).[50]

The calculations consistently establish a progressive stabilization of the HS/LS configuration upon increasing the water molecule content (Table S6†). The energy difference between HS/LS and LS configurations ($\Delta E_{HS/LS-LS}$) increases from 0.515 eV for the dehydrated phase to 0.356 eV for the system calculated with six water molecules (see Table S6† for details). Interaction and steric effects upon increase of water content yield to a progressive increase of the benzene torsion together with an increase in the average Fe-N bond lengths and unit cell volume (see Table S7).

## Conclusions

Our findings reveal that the pores of MOF **1** contain two distinct populations of guest water molecules: O1w, which strongly interacts with the framework of **1**, and O2w and O3w, which have weaker interactions. This results in O2w and O3w water molecules being readily adsorbed and desorbed from the pores, while O1w water molecules remain tightly bound and requires harsher conditions for removal.

This water uptake/release behaviour in **1** induces the HS to LS transition in **1**, in a reverse spin crossover phenomenon. Above 300 K, MOF **1** undergoes a transition from the HS/LS state to the LS state. At these temperatures, guest water molecules (*i.e.,* O2w and O3w water types) are released from the pores of **1**, inducing flexibility to the frameworks, accompanied by a volume contraction and a change of the configuration of the benzene ring within the organic linker. This suggests a dynamic adaptation of the framework through phenyl ring rotations, leading to a significant decrease in SAV (**1**$^{300}$→**1**$^{350}$). Upon complete conversion to the LS state (**1**$^{350}$→**1**$^{420}$) at high temperature, where MOF **1** is almost dehydrated (a percentage of O1w water type is still observed), the position of the phenyl rings is more restrained, resulting in a higher SAV despite the lower framework volume. DFT calculations support these experimental observations, demonstrating a progressive stabilization of the LS configuration with decreasing water content which is concomitant with a shortening of Fe-N bond lengths and a smaller torsion of the benzene rings. This highlights the interplay between water molecules and the SCO process, with water loss facilitating the transition to the LS state.

The reverse SCO, as observed in the example presented here, represents a new resource for the design of switchable advanced materials. Furthermore, this work reveals a counter-intuitive process where the expected increase in positional freedom of phenyl ligands, due to water molecule evacuation from MOF pores, is outweighed by the immobilizing effect of the reverse spin crossover (SCO) from high-spin (HS) to low-spin (LS). This outcome is highly significant for both the spin-crossover and MOF research communities, as it highlights an unexpected dominance of the spin-transition effect, providing new insights into ligand dynamics and the interactions between spin states and structural flexibility within MOF materials. This knowledge could lead to the development of more precise and responsive materials for applications in areas such as molecular switches, data storage, and smart sensors, where the ability to control ligand dynamics through spin state manipulation could offer significant advantages.[51–53].

## Author contributions

A.M-M.: Synthesis of compounds, A.M-M., E.R-U. J.A. and D.M.: Characterization of compounds. E.C.S.: SCXRD Refinement and electron density studies. J.A.R-V.: SCXRD measurements. A.L.M and R.P.: DFT calculations. J.S.C., E.R-U and A.M-M.: Writing. J.S.C.: Funding and supervision.

## Conflicts of interest

There are not conflicts to declare.

## Data availability

A data availability statement (DAS) is required to be submitted alongside all articles. Please read our full guidance on data availability statements for more details and examples of suitable statements you can use.

## Acknowledgements

JSC thanks funds from the Spanish MICINN through National Research Project (PID2020114653RB-I00 and TED2021-131018B-C22) and the MAD2D-CMMRR MATERIALES AVANZADOS-IMDEANC-4. AM-M thanks funds from the Spanish MICINN through PRE2019-C-87849. IMDEA Nanociencia acknowledges support from the 'Severo Ochoa' Programme for Centres of Excellence in R&D (MINECO, Grant CEX2020-001039-S). ECS ackowledges financial support from the Spanish Governement, Ministerio de Ciencia e Innovación projects Generación del Conocimiento PGC2018-098630-B-I00 and PID2022-137764OB-I00. We thank the XALOC-ALBA synchrotron source under project 2023017235.

## Notes and references

1 H. Furukawa, K. E. Cordova, M. O'Keeffe and O. M. Yaghi, *Science*, 2013, **341**, 1230444.

2 M. Dincă, A. F. Yu and J. R. Long, *J. Am. Chem. Soc.*, 2006, **128**, 8904–8913.

3 W. Fan, X. Zhang, Z. Kang, X. Liu and D. Sun, *Coord. Chem. Rev.*, 2021, **443**, 213968.

4 F.-F. Yan, W.-J. Jiang, N.-T. Yao, P.-D. Mao, L. Zhao, H.-Y. Sun, Y.-S. Meng and T. Liu, *Chem. Sci.*, 2023, **14**, 6936–6942.

5 F. Bigdeli, C. T. Lollar, A. Morsali and H. Zhou, *Angew. Chem. Int. Ed.*, 2020, **59**, 4652–4669.

6 M. C. Muñoz and J. A. Real, *Coord. Chem. Rev.*, 2011, **255**, 2068–2093.

7 D. Aguilà, Y. Prado, E. S. Koumousi, C. Mathonière and R. Clérac, *Chem. Soc. Rev.*, 2016, **45**, 203–224.

8 W. S. Drisdell, R. Poloni, T. M. McDonald, J. R. Long, B. Smit, J. B. Neaton, D. Prendergast and J. B. Kortright, *J. Am. Chem. Soc.*, 2013, **135**, 18183–18190.

9 Y. Shen, J. Woodburn, S. Bouras, S. Dai, I. Dovgaliuk, J.-M. Grenèche, G. Patriarche, L. M. Lawson Daku, C. Serre and A. Tissot, *Chem. Mater.*, 2023, **35**, 719–727.

10 P. Gütlich, A. B. Gaspar and Y. Garcia, *Beilstein J. Org. Chem.*, 2013, **9**, 342–391.

11 Y. Shen, A. Tissot and C. Serre, *Chem. Sci.*, 2022, **13**, 13978–14007.

12 E. Resines-Urien, E. Fernandez-Bartolome, A. Martinez-Martinez, A. Gamonal, L. Piñeiro-López and J. Sanchez Costa, *Chem. Soc. Rev.*, 2023, **52**, 705–727.

13 E. Resines-Urien, M. Á. García García-Tuñón, M. García-Hernández, J. A. Rodriguez-Velamazan, A. Espinosa and J. Sanchez Costa, *Adv. Sci.*, 2022, **9**, 2202253.

14 Y. Zhao, Z. Song, X. Li, Q. Sun, N. Cheng, S. Lawes and X. Sun, *Energy Storage Mater.*, 2016, **2**, 35–62.

15 A. Martinez-Martinez, E. Resines-Urien, N. S. Settineri, S. J. Teat, E. C. Sañudo, O. Fabelo, J. A. Rodriguez-Velamazan, L. Piñeiro-López and J. Sanchez Costa, *Cryst. Growth Des.*, 2023, **23**, 3952–3957.

16 G. A. Craig, J. Sanchez Costa, O. Roubeau, S. J. Teat, H. J. Shepherd, M. Lopes, G. Molnár, A. Bousseksou and G. Aromí, *Dalton Trans.*, 2014, **43**, 729–737.

17 S. Bonhommeau, T. Guillon, L. M. Lawson Daku, P. Demont, J. Sanchez Costa, J.-F. Létard, G. Molnár and A. Bousseksou, *Angew. Chem. Int. Ed.*, 2006, **45**, 1625–1629.

18 J.-F. Létard, P. Guionneau, O. Nguyen, J. Sanchez Costa, S. Marcén, G. Chastanet, M. Marchivie and L. Goux-Capes, *Chem. Eur. J.*, 2005, **11**, 4582–4589.

19 C. Bartual-Murgui, L. Salmon, A. Akou, N. A. Ortega-Villar, H. J. Shepherd, M. C. Muñoz, G. Molnár, J. A. Real and A. Bousseksou, *Chem. Eur. J.*, 2012, **18**, 507–516.

20 W.-B. Chen, Y.-C. Chen, M. Yang, M.-L. Tong and W. Dong, *Dalton Trans.*, 2018, **47**, 4307–4314.

21 J. Sanchez Costa, S. Rodríguez-Jiménez, G. A. Craig, B. Barth, C. M. Beavers, S. J. Teat and G. Aromí, *J. Am. Chem. Soc.*, 2014, **136**, 3869–3874.

22 K. Senthil Kumar and M. Ruben, *Coord. Chem. Rev.*, 2017, **346**, 176–205.

23 V. Rubio-Giménez, S. Tatay and C. Martí-Gastaldo, *Chem. Soc. Rev.*, 2020, **49**, 5601–5638.

24 G. Molnár, S. Rat, L. Salmon, W. Nicolazzi and A. Bousseksou, *Adv. Mater.*, 2018, **30**, 1703862.

25 M. Weselski, M. Książek, P. Mess, J. Kusz and R. Bronisz, *Chem. Commun.*, 2019, **55**, 7033–7036.

26 F. J. Valverde-Muñoz, M. Seredyuk, M. C. Muñoz, G. Molnar, Y. S. Bibik and J. A. Real, *Angew. Chem. Int. Ed.*, 2020, **59**, 18632–18638.

27 E. Resines-Urien, E. Burzurí, E. Fernandez-Bartolome, M. Á. García García-Tuñón, P. de la Presa, R. Poloni, S. J. Teat and J. Sanchez Costa, *Chem. Sci.*, 2019, **10**, 6612–6616.

28 N. F. Sciortino, F. Ragon, Y. M. Klein, C. E. Housecroft, C. G. Davies, G. N. L. Jameson, G. Chastanet and S. M. Neville, *Inorg. Chem.*, 2018, **57**, 11068–11076.

29 B. E. R. Snyder, A. B. Turkiewicz, H. Furukawa, M. V. Paley, E. O. Velasquez, M. N. Dods and J. R. Long, *Nature*, 2023, **613**, 287–291.

30 H. J. Windsor, W. Lewis, S. M. Neville, S. G. Duyker, D. M. D'Alessandro and C. J. Kepert, *Chem. Commun.*, 2022, **58**, 13127–13130.

31 K. A. Zenere, S. G. Duyker, E. Trzop, E. Collet, B. Chan, P. W. Doheny, C. J. Kepert and S. M. Neville, *Chem. Sci.*, 2018, **9**, 5623–5629.

32 R. Turo-Cortés, C. Bartual-Murgui, J. Castells-Gil, M. C. Muñoz, C. Martí-Gastaldo and J. A. Real, *Chem. Sci.*, 2020, **11**, 11224–11234.

33 M. Ohba, H. Ando, N. Yoshihide, S. Shigeyoshi and S. Kitagawa, *Angew. Chem. Int. Ed.*, 2009, **48**, 4767–4771.

34 N. F. Sciortino, F. Ragon, K. A. Zenere, P. D. Southon, G. J. Halder, K. W. Chapman, L. Piñeiro-López, J. A. Real, C. J. Kepert and S. M. Neville, *Inorg. Chem.*, 2016, **55**, 10490–10498.

35 C. Bartual-Murgui, A. Akou, H. J. Shepherd, G. Molnár, J. A. Real, L. Salmon and A. Bousseksou, *Chem. Eur. J.*, 2013, **19**, 15036–15043.

36 Y. Imamura, H. Yoshino, B. Le Ouay, R. Ohtani and M. Ohba, *Dalton Trans.*, 2024, **53**, 3970–3974.

37 Y. Han, P. Das, Y. He, D. C. Sorescu, K. D. Jordan and N. L. Rosi, *J. Am. Chem. Soc.*, 2022, **144**, 19567–19575.

38 P. D. Southon, L. Liu, E. A. Fellows, D. J. Price, G. J. Halder, K. W. Chapman, B. Moubaraki, K. S. Murray, J.-F. Létard and C. J. Kepert, *J. Am. Chem. Soc.*, 2009, **131**, 10998–11009.

39 K.-T. Lian, W.-W. Wu, G.-Z. Huang, Y. Liu, S.-G. Wu, Z.-P. Ni and M.-L. Tong, *Inorg. Chem. Front.*, 2021, **8**, 4334–4340.

40 T. Gebretsadik, Q. Yang, J. Wu and J. Tang, *Coord. Chem. Rev.*, 2021, **431**, 213666.

41 Z. Feng, J.-J. Ling, H. Song and D. Zhu, *Inorg. Chem. Front.*, 2023, **10**, 305–315.

42 Z. Yan, M. Li, H.-L. Gao, X.-C. Huang and D. Li, *Chem. Commun.*, 2012, **48**, 3960–3962.

43 W.-T. Liu, J.-Y. Li, Z.-P. Ni, X. Bao, Y.-C. Ou, J.-D. Leng, J.-L. Liu and M.-L. Tong, *Cryst. Growth Des.*, 2012, **12**, 1482–1488.

44 A. Martinez-Martinez, E. Resines-Urien, L. Piñeiro-López, A. Fernández-Blanco, A. Lorenzo Mariano, J. Albalad, D. Maspoch, R. Poloni, J. A. Rodríguez-Velamazán, E. C. Sañudo, E. Burzurí and J. Sanchez Costa, *Chem. Mater.*, 2023, **35**, 6012–6023.

45 J.-P. Xue, Y. Hu, B. Zhao, Z.-K. Liu, J. Xie, Z.-S. Yao and J. Tao, *Nat. Commun.*, 2022, **13**, 3510.

46 R. Vismara, S. Terruzzi, A. Maspero, T. Grell, F. Bossola, A. Sironi, S. Galli, J. A. R. Navarro and V. Colombo, *Adv. Mater.*, 2024, **36**, 2209907.

47 X. Chen, H. Xie, E. R. Lorenzo, C. J. Zeman, Y. Qi, Z. H. Syed, A. E. B. S. Stone, Y. Wang, S. Goswami, P. Li, T. Islamoglu, E. A. Weiss, J. T. Hupp, G. C. Schatz, M. R. Wasielewski and O. K. Farha, *J. Am. Chem. Soc.*, 2022, **144**, 2685–2693.

48 A. L. Spek, *Acta Crystallogr. C Struct. Chem.*, 2015, **71**, 9–18.

49 J. A. Rodríguez-Velamazán, M. A. González, J. A. Real, M. Castro, M. C. Muñoz, A. B. Gaspar, R. Ohtani, M. Ohba, K. Yoneda, Y. Hijikata, N. Yanai, M. Mizuno, H. Ando and S. Kitagawa, *J. Am. Chem. Soc.*, 2012, **134**, 5083–5089.

50 L. A. Mariano, B. Vlaisavljevich and R. Poloni, *J. Chem. Theory Comput.*, 2021, **17**, 2807–2816.

51 L. Kipgen, M. Bernien, F. Tuczek and W. Kuch, *Adv. Mater.*, 2021, **33**, 2008141.

52 J. Villalva, A. Develioglu, N. Montenegro-Pohlhammer, R. Sánchez-de-Armas, A. Gamonal, E. Rial, M. García-Hernández, L. Ruiz-Gonzalez, J. Sanchez Costa, C. J. Calzado, E. M. Pérez and E. Burzurí, *Nat. Commun.*, 2021, **12**, 1578.

53 R. Torres-Cavanillas, M. Gavara-Edo and E. Coronado, *Adv. Mater.*, 2024, **36**, 2307718.